ACS APPLIED MATERIALS & INTERFACES

www.acsami.org

Research Article

Monitor Tumor pHe and Response Longitudinally during Treatment Using CEST MRI-Detectable Alginate Microbeads

Peng Xiao, Jianpan Huang, Xiongqi Han, Jacinth W. S. Cheu, Yang Liu, Lok Hin Law, Joseph H. C. Lai, Jiyu Li, Se Weon Park, Carmen C. L. Wong, Raymond H. W. Lam, and Kannie W. Y. Chan*

Cite This: *ACS Appl. Mater. Interfaces* 2022, 14, 54401−54410

Read Online

ACCESS | Metrics & More | Article Recommendations | Supporting Information

ABSTRACT: Imaging pHe of the tumor microenvironment has paramount importance for characterizing aggressive, invasive tumors, as well as therapeutic responses. Here, a robust approach to image pH changes in the tumor microenvironment longitudinally and during sodium bicarbonate treatment was reported. The pH-sensing microbeads were designed and prepared based on materials approved for clinical use, i.e., alginate microbead-containing computed tomography (CT) contrast-agent (iopamidol)-loaded liposomes (Iop-lipobeads). This Iop-lipobead prepared using a customized microfluidic device generated a CEST contrast of 10.6% at 4.2 ppm at pH 7.0, which was stable for 20 days in vitro. The CEST contrast decreased by 11.8% when the pH decreased from 7.0 to 6.5 in vitro. Optimized Iop-lipobeads next to tumors showed a significant increase of 19.7 ± 6.1% ($p < 0.01$) in CEST contrast at 4.2 ppm during the first 3 days of treatment and decreased to 15.2 ± 4.8% when treatment stopped. Notably, percentage changes in Iop-lipobeads were higher than that of amide CEST (11.7% and 9.1%) in tumors during and after treatment. These findings demonstrated that the Iop-lipobead could provide an independent and sensitive assessment of the pHe changes for a noninvasive and longitudinal monitoring of the treatment effects using multiple CEST contrast.

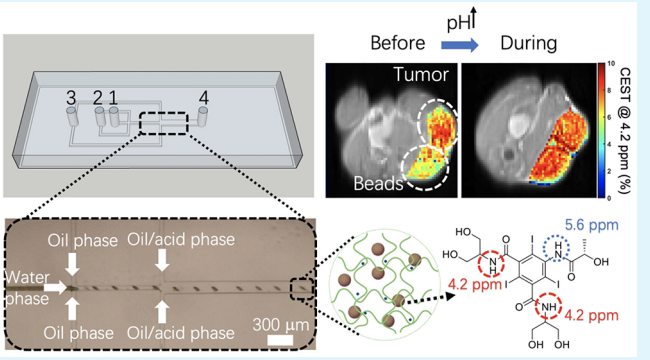

KEYWORDS: *CEST, microfluidics, pH monitor, Iopamidol, bicarbonate treatment*

INTRODUCTION

Acidosis is one of the hallmarks of the tumor microenvironment; i.e., pHe is approximately 6.3 to 6.9, which could cause resistance to immunotherapy as well as some chemotherapies and radiotherapy.[1−7] This is related to the production and accumulation of lactic acid via aerobic glycolysis, hypoxia, poor perfusion of tumor cells, and poor buffering.[8,9] Thus, monitoring the tumor pHe is of paramount importance in diagnosis and therapy. Conventional pH imaging requires the administration of pH sensitive dyes, contrast agents (CAs), or tracers,[10,11] such as dyes in fluorescence imaging[12] and photoacoustic imaging,[13] and tracers in positron emission tomography (PET) imaging,[14] to enhance the sensitivity of detecting local pH changes in the heterogeneous tumor environments. Numerous magnetic resonance imaging (MRI) approaches that could reveal tumor pH, including MR spectroscopy[15−17] and emerging chemical exchange saturation transfer (CEST), have been applied for imaging acidosis with[18] or without[19] CAs. The emerging MR approaches could solve the limitations associated with spatial and temporal resolution, especially CEST MRI that enables the use of endogenous contrast and/or exogeneous agents approved for clinical use to support frequent assessments. For example, the natural exchangeable protons of computed tomography (CT) CAs have been successfully repurposed as pH-sensitive CEST CAs for tumor pH imaging.[20,21] The endogenous CEST contrast of tumors, such as the amide proton transfer (APT) at around 3.5 ppm, has been applied to identify acute stroke[22] and radiation necrosis from tumor recurrence.[23−25] APT is more sensitive to alterations in the concentration of proteins than pH, thus it will be challenging to monitor pHe independently using an endogenous APT signal.[26,27]

CT CAs, such as iopamidol, have been exploited for CEST-MRI pH imaging to monitor tumor pH in both preclinical[28,29] and clinical[30] applications. Many advantages in tumor imaging have been demonstrated since the first report of CEST properties of CT contrast agents by Aime et al. in 2005.[31−33] First, the delivery of CT CA can generate as high as 10% CEST contrast at 4.2 ppm[20] and detect pH with a precision of 0.07 in

Received: June 13, 2022
Accepted: October 5, 2022
Published: November 30, 2022

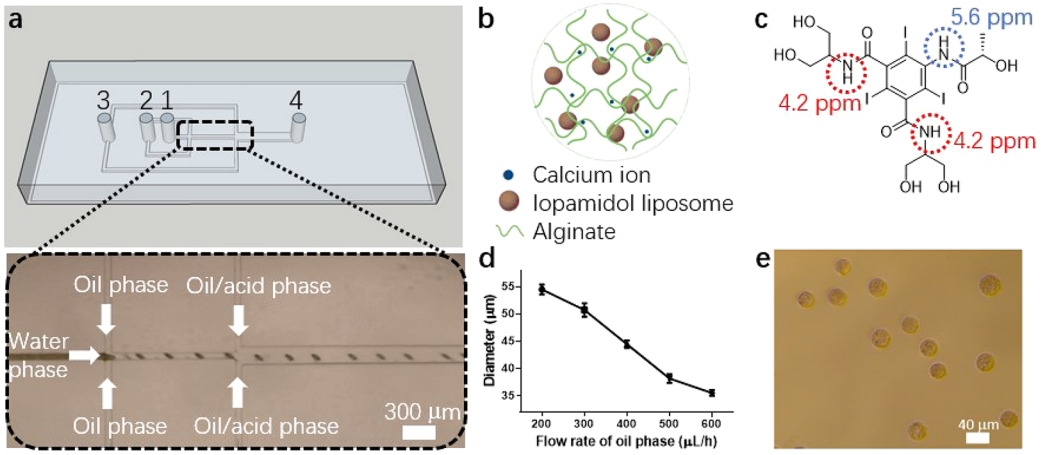

Figure 1. Microfluidic fabrication of alginate microbeads incorporated with iopamidol-loaded liposome (Iop-lipobeads). (a) Microfluidic design for the preparation of microbeads. 1, 2, and 3 are inlets for the water phase, oil phase, and oil/acid phase, respectively, and 4 is the outlet. (b) Schematic of Iop-lipobeads. (c) Chemical structure of iopamidol showing exchangeable amide protons generating CEST at 4.2 and 5.6 ppm. (d) Oil phase flow rate dependency of Iop-lipobead size. Iop-lipobead size decreased with the increased flow rate of oil phase when water flow rate and oil/acid flow rate were set at 120 μL/h and 1500 μL/h, respectively. The error bars represent the standard error of the mean. (e) Bright field image of Iop-lipobeads prepared at an oil flow rate of 600 μL/h.

the range of 6.2−7.4.[18] Second, acidoCEST using iopamidol showed a higher contrast-to-noise ratio than endogenous APT CEST in pH measurements.[34] Third, they can be used to monitor tumor pHe for the assessment of treatment effects, such as bicarbonate treatment,[18] dichloroacetate treatment,[35] and metformin treatment.[29] This pH imaging approach has been successfully applied in differentiating pancreatitis and pancreatic cancer,[36] assessing lung cancer,[37] and breast cancer.[38]

In order to address the clinical needs for sensitive and pHe-specific imaging during the course of treatment. There is a need to develop alternative pHe monitoring approaches that are free of high dose and repeated administration of CAs, which could lead to nephrotoxicity.[39] Alginate microbeads have been widely used in the delivery of cells, drugs, and agents due to their biocompatibility, inertness, and ease of fabrication.[40−42] A previous CEST study demonstrated that these alginate microbeads could sensitively detect subtle changes in local pH when cell death occurs.[43] While these alginate microbeads at around 300−400 μm prepared by electrospray[51] generated a stable CEST contrast in vitro for about a month,[43] a more controllable preparation that generates microbeads with monodispersity, small and spherical alginate microbeads could minimize the immune responses,[44] such as the foreign body responses.[45,46] Microfluidic fabrication could provide these advantages in the preparation of alginate microbeads with monodispersed size.[40,47]

In this study, we aim to develop a microfluidic platform to generate CT CA containing alginate microbeads with high CEST contrast and pH sensitivity, and high CA retention for longitudinal tumor CEST pHe imaging during treatment. Presumably the observed changes in CEST of these microbeads could indicate the changes in pHe not in amide concentration. We designed a robust microfluidic device for the fabrication of alginate microbeads containing liposomes loaded with iopamidol (Iop-lipobeads) in tens of microns. Then, we studied the CEST properties of Iop-lipobeads and applied the Iop-lipobeads to monitor the subcutaneous tumor pHe longitudinally at 3T during sodium bicarbonate treatment. We monitored and compared both the CEST contrast from Iop-lipobeads and endogenous CEST contrast of tumors for multiple CEST contrast imaging.

MATERIALS AND METHODS

Materials. Sodium alginate (PRONOVA UP LVM) was purchased from NovaMatrix (Norway). All lipids were purchased from Avanti Polar Lipids, Inc. (Alabaster, AL, USA). Ethylenediamine tetra-acetic acid disodium salt dihydrate (Na_2EDTA) and calcium chloride anhydrous were purchased from Sinopharm Chemical Reagent Co., Ltd. (Shanghai, China). Sodium chloride was purchased from Dieckmann (China). Mineral oil and trichloro(1H,1H,2H,2H-perfluoro-octyl) silane were purchased from Sigma (Sigma-Aldrich, Milwaukee, WI). Negative photoresist SU-8 2050 and SU8 developer were obtained from Chestech (Rugby, UK). Polydimethylsiloxane (PDMS) prepolymer and the curing agent (Sylgard 184) were obtained from Dow Corning (Midland, MI, USA). Sephadex G50 columns were purchased from GE Healthcare Life Sciences (Pittsburgh, PA). Dulbecco's Minimum Essential Medium (DMEM, GlutaMAXTM-1) and DMEM-HG medium were purchased from Gibco, Invitrogen.

Design and Fabrication of Microfluidic Device. Two cross-junctions were designed for the alginate microbead formation. The first cross-junction with a 50 μm width and 50 μm height was used for the alginate droplet generation, and the second cross-junction was designed for introducing acetic acid into the channel to release ions for cross-linking. Microfluidic devices were fabricated by soft lithography and replica modeling of PDMS.[48,49] Negative photoresist SU-8 was spun and coated onto a clean silicon wafer with a thickness of 50 μm and patterned by UV exposure through a transparency photomask. After developing the microstructure, the wafer was deposited with trichloro (1H,1H,2H,2H-perfluoro-octyl) saline. A degassed mixture of PDMS and curing agent (at 10:1) was poured onto the pattern and cured at 65 °C for 2 h. The PDMS molds were then peeled off the master and punched for the channel inlets and outlet. The PDMS replicates were bonded to glass slides after plasma activation of both surfaces and cured overnight at 65 °C to enhance bonding.

Preparation and Characterization of Iopamidol-Loaded Liposome. The thin film hydration method was used to prepare iopamidol-loaded liposome.[50] In brief, 50 mg of egg phosphatidylcholine (PC), DSPC-PEG-2000, and cholesterol were mixed in a molar ratio of 24:3:73 in chloroform. The resulted thin film was hydrated with 1 mL of iopamidol solution at 972 mM. The suspension was annealed at 55 °C for 1 h. Liposomes were obtained after sonication and extrusion through polycarbonate filters with 400 μm pores. Unencapsulated iopamidol was removed by passing through Sephadex twice. Liposome

https://doi.org/10.1021/acsami.2c10493
ACS Appl. Mater. Interfaces 2022, 14, 54401−54410

size and zeta potential were measured by Zetasizer (Malvern Instruments), while the liposome concentration was measured by Nanosight (Malvern Instruments).

Preparation of Liposome Incorporated Alginate Hydrogel Microbeads Using Microfluidics. First, 2 w/v% sodium alginate powder was dissolved in 100 mM Ca-EDTA solution followed by pH adjustment to 7.4 using sodium hydroxide to form Alg-Ca-EDTA solution. The water phase was composed of liposome and Alg-Ca-EDTA solution and mixed at a volume ratio of 1:1. The oil phase and oil/acid phase were composed of mineral oil with 2 wt % Span 80 and mineral oil with 3 wt % Span 80 and 1.5 v/v% acetic acid, respectively. Acetic acid was used to trigger the release of calcium ions from the Ca-EDTA complex for hydrogel bead formation.

To fabricate Iop-lipobeads, the water phase, oil phase, and oil/acid phase were pumped into the device via inlets 1, 2, and 3, respectively (Figure 1a). Droplets were generated at the first cross-junction. An oil/acid phase containing acetic acid coflowed with the formed droplets at the second cross-junction. As a result, the acid triggered the release of Ca^{2+} from the Ca-EDTA complex and initiated the cross-linking of the alginate droplet. The flow rate of the oil phase was adjusted from 200 μL/h to 600 μL/h to achieve different sizes of Iop-lipobeads (Figure S1) when both flow rates for the water phase and oil/acid phase were fixed at 120u μL/h and 1500 μL/h, respectively. After droplet formation, alginate microbeads were collected in a vial containing saline solution (20 mM $CaCl_2$ in 0.9 wt % NaCl solution). The beads were then washed with saline solution at 37 °C to remove the oil on microbeads.

CEST Imaging. All MRI experiments were performed on a horizontal bore 3T preclinical Bruker MRI system (Bruker, Ettlingen, Germany). For Iop-lipobead phantom imaging, a 40 mm transmitting and receiving volume coil was used. The B_0 field was shimmed to the second-order using water line width. A modified rapid acquisition with a relaxation enhancement (RARE) sequence with a continuous-wave presaturation pulse was used to acquire CEST images at different irradiation frequencies. Imaging parameters were set as follows: slice thickness = 2 mm, field of view (FOV) = 20 × 20 mm, image size = 64 × 64, RARE factor = 32, repetition time (TR) = 6000 ms, echo time (TE) = 86.77 ms, resulting in an acquisition time of 12.0 s for each offset. One slice from coronal orientation was selected for CEST acquisition. CEST frequency varied from −20 to 20 ppm, with a step of 0.1 ppm between −1 and 1 ppm, a step of 0.2 ppm between ±1 and ±8 ppm, and a step of 0.5 ppm between ±8 and ±11 ppm. Four M_0 images at 200 ppm were acquired for Z-spectrum normalization. Thus, the total scan time of a CEST acquisition was 21 min 24 s with −11 to 11 ppm for the test of power optimization, pH dependency, and CEST retention. For the medium test, extra acquisition points on ±13, ±15, and ±20 ppm were acquired, resulting in a total scan time of 22 min 36 s. The saturation power (B_1) was varied as 0.6, 0.8, 1.2, 1.6, 2.0, and 3.0 μT with a constant saturation duration (T_{sat}) of 3 s to optimize the saturation parameters. The data were processed using custom-written MatLab (Mathworks, Natick, MA) scripts. The Z-spectra were calculated using the mean of each region of interest (ROI) placed over each sample after B_0 correction on a pixel-wise basis. CEST contrast (%) was quantified by subtracting Z-spectra from the Lorentzian fitted water and magnetization transfer signal.[51,52]

For the in vivo CEST MRI, some parameters were different with in vitro CEST MRI. A 23 mm transmitting and receiving volume coil was used. Imaging parameters were the same as described above for in vitro imaging except for the following: slice thickness = 1.5 mm, FOV = 25 × 25 mm, TR = 5000 ms, TE = 6.9 ms, resulting in an acquisition time of 10 s for each offset and a total acquisition time of 18 min 50 s (−20 ppm to 20 ppm as mentioned above). The B_1 was varied at 0.6, 0.8, 1.2, 1.6, and 2.0 μT to optimize the saturation parameters.

Preparation of Phantoms for pH Sensitivity Measurement. pH phantoms at 6.0, 6.5, 7.0, 7.5, and 8.0 pH were prepared using saline solution, and the pH was adjusted by diluted hydrochloric acid and sodium hydroxide. Hypoxic medium (HM) and normoxic medium (NM) were obtained from mediums cultured with MHCC97L cells in a hypoxia incubator chamber (Billups-Rothenberg) with 1% and 20% O_2, both for 24 h, respectively. Fresh medium (FM) was the medium without cell culture. The pH of HM, NM, and FM were measured and found to be at 6.8, 7.1, and 7.2, respectively, before mixing with Iop-lipobeads. A total of 150 μL of Iop-lipobeads was mixed with 300 μL of each medium, followed by centrifugation at 1000 rpm for 1 min before CEST measurement. Then, the CEST contrast of the medium phantom was measured using the same imaging protocol described in CEST imaging section.

Preparation of Tumor Mouse Model, Iop-Lipobeads Injection, and Bicarbonate Treatment. Female nude mice (4−8 weeks, n = 9) were acquired from the Laboratory Animal Research Unit at City University of Hong Kong. All in vivo studies were conducted according to procedures approved by the institutional ethical review of research experiments involving animal subjects committee. To implant tumors, the mice received a subcutaneous injection of a 100 μL suspension of U87 cells with a cell number of 5×10^6 at the dorsal aspect of the right posterior limb. The pHe at the tumor periphery can well represent the aggressiveness of the tumor.[1,53] Moreover, the injection of microbeads into the center of the tumor could perturb the tumor structure due to intratumoral pressure of the solid tumors. Thus, when tumor volume grew up to ∼150 mm^3, 300 μL of sterilized microbeads were subcutaneously injected near the tumor.

The bead injection day was marked as day 0. Two days later, drinking water was replaced with 200 mM autoclaved sodium bicarbonate solution for the tumor treatment group (n = 5). The bicarbonate solution was replaced with normal drinking water after a 3-day treatment. For the control group (n = 4), microbeads were subcutaneously injected into the mice without tumors, and the mice received the same bicarbonate treatment as the treatment group. CEST MRI was performed from day 1 to day 7 daily. Mice were first anesthetized using 2% isoflurane for induction and then maintained using 1.0−1.5% isoflurane during MRI. The body temperature was maintained using a warming pad, and the respiration was monitored by a respiratory pad connected to a monitoring system (SA Instrument, NY, USA). Imaging parameters were the same as those described in the previous CEST imaging section.

Histology Analysis. Tumor and bead areas were harvested after all CEST monitoring experiments and postfixed in 4% paraformaldehyde (PFA) solution, then transferred to 30 wt % sucrose solution and kept at 4 °C. Histological sections with a 16 μm thickness were obtained using a cryostat and directly mounted onto microscopic slides. Histological analysis was performed by hematoxylin and eosin (H&E) staining according to the standard protocols.[54,55]

RESULTS AND DISCUSSIONS

Design and Preparation of Iop-Lipobeads Using Customized Microfluidic Device. To maintain a sustainable CEST contrast, iopamidol was first encapsulated in liposomes with 73 mol % of cholesterol. This high concentration of cholesterol could improve the retention of intraliposomal agents.[43,56] Then, the iopamidol encapsulated liposomes were incorporated into the alginate hydrogel beads using a flow-focusing microfluidic device (Figure 1a). The microfluidic device had three inlets and one outlet coupled with internal gelation (Figure 1a). This enabled the generation of Iop-lipobeads with a homogeneous size and spherical shape as shown in Figures 1e and S1. The increase in the flow rate of the oil phase from 200 to 600 μL/h resulted in a decrease of the average alginate particle size from 54.5 to 35.6 μm (Figures 1d,e and S1). The design of Iop-lipobeads is shown in Figure 1b, the high concentration of iopamidol-loaded liposomes (i.e., 10^{17} particles per mL) premixed with alginate at the water phase enabled a homogeneous distribution of liposomes in Iop-lipobeads and a high concentration of iopamidol for CEST MRI. Since a smaller particle size with a high surface-to-volume ratio could improve the water accessibility for CEST MRI,[44,57] Iop-lipobeads of 35.6 ± 4.6 μm were used for further experiments.

https://doi.org/10.1021/acsami.2c10493
ACS Appl. Mater. Interfaces 2022, 14, 54401−54410

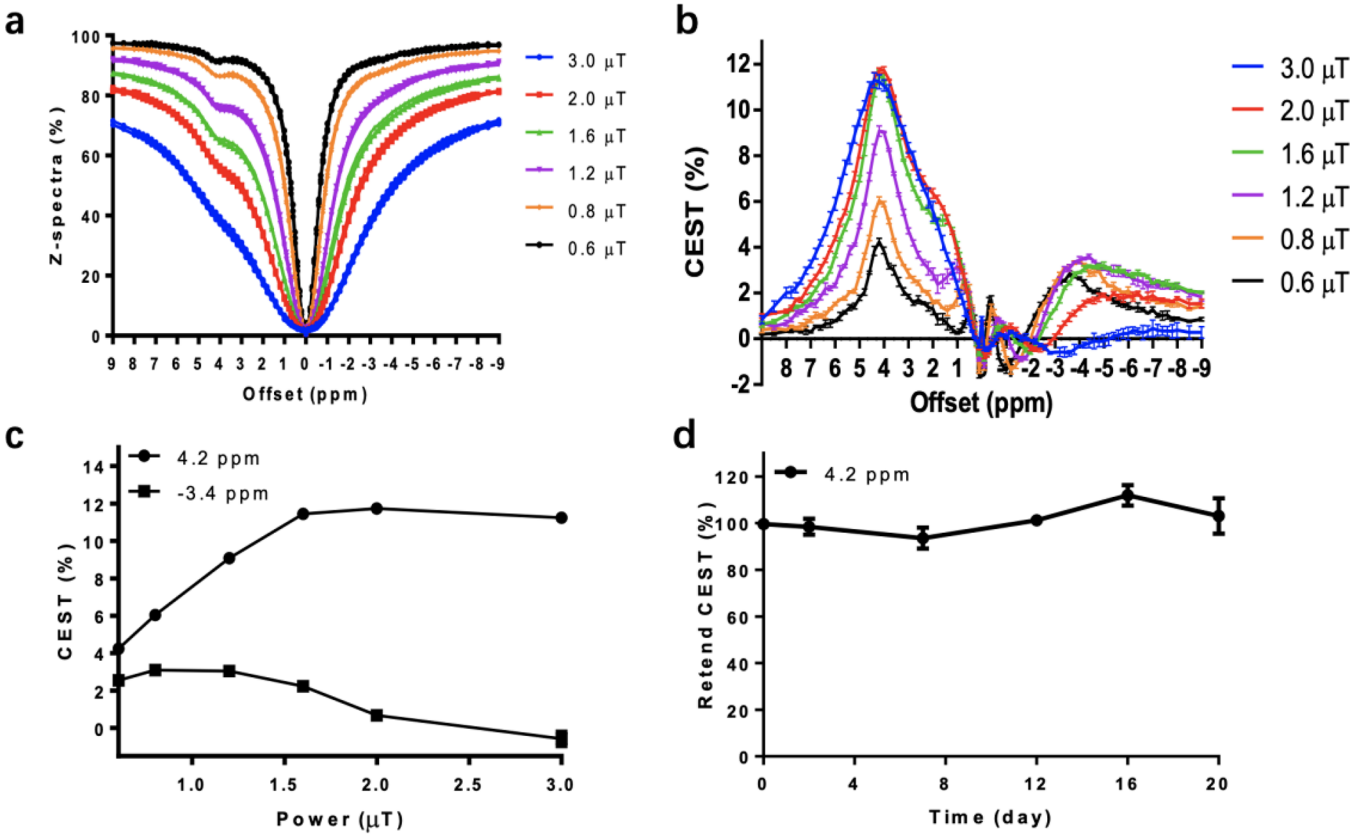

Figure 2. CEST imaging parameter optimization for Iop-lipobeads and stability of CEST contrast over time. (a) Z-spectra and (b) CEST contrast for Iop-lipobeads at B_1 values of 0.6, 0.8, 1.2, 1.6, 2.0, and 3.0 μT, and at T_{sat} = 3 s and 37 °C. (c) B_1 power dependency of CEST contrast at 4.2 ppm and −3.4 ppm, showing that CEST contrast at 4.2 ppm reached the highest value at 1.6 and 2.0 μT. (d) Time course of CEST contrast at 4.2 ppm in Iop-lipobeads with daily replacement of saline at 37 °C showed the stability. CEST was measured at 1.6 μT and normalized to day 0. The error bars represent the standard error of the mean.

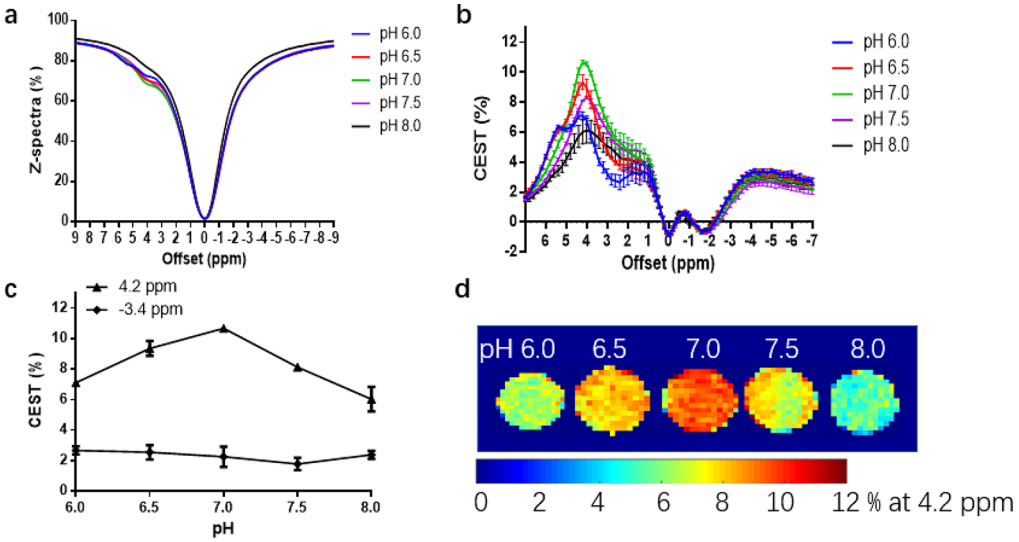

Figure 3. pH dependency of Iop-lipobeads in a pH range of 6.0 to 8.0. CEST contrast at 4.2 ppm increased with pH and reached the highest value at pH 7.0 at 1.6 μT. (a) Z-spectra and (b) CEST contrast for Iop-lipobeads. (c) pH dependency of CEST contrast at 4.2 ppm and −3.4 ppm. (d) The CEST maps at 4.2 ppm. The error bars represent standard errors.

Characterization of Iopamidol-Loaded Liposome. The average size of iopamidol loaded liposomes was 200 nm with a polydispersity index (PDI) of 0.27, and the corresponding Zeta potential and particle concentration were −0.5 mV and (1.6 ± 0.3) × 10^{17} /mL, respectively. Liposomes at this size were chosen due to the favorable membrane water exchange rate[44] and sustainable retention in alginate cross-linked hydrogel.[58] Z-spectra and CEST contrast acquired at pH 7, 37 °C, and 3T are shown in Figure S2. Under a B_1 of 1.6 μT, the CEST contrast of liposomes was 42.4 ± 1.3% at 4.2 ppm and 1.8 ± 0.4% at −3.4

https://doi.org/10.1021/acsami.2c10493
ACS Appl. Mater. Interfaces 2022, 14, 54401−54410

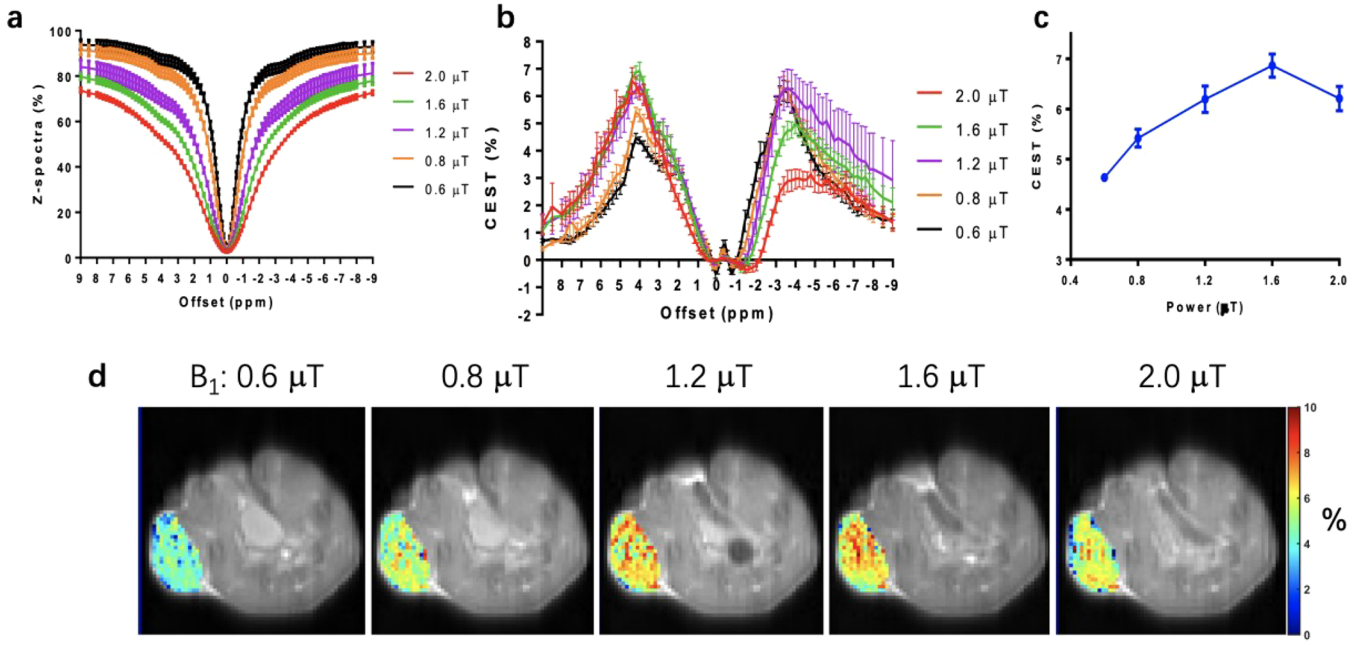

Figure 4. Power optimization for CEST imaging of Iop-lipobeads in mice without a tumor at day 2 (n = 4). (a) Z-spectra and (b) CEST contrast for Iop-lipobeads at B_1 of 0.6, 0.8, 1.2, 1.6, and 2.0 μT. (c) B_1 power dependency of CEST contrast at 4.2 ppm, showing that CEST contrast at 4.2 ppm reached the highest value at 1.6 μT. (d) Representative CEST map at 4.2 ppm of Iop-lipobeads at different B_1 powers. The error bars represent standard errors.

ppm, which were attributed to the amide protons on iopamidol[31] and the aliphatic protons on liposomes, respectively.[51]

CEST Contrast of Iop-lipobeads in Vitro. CEST contrast of Iop-lipobeads at 35.6 ± 4.6 μm prepared via microfluidic device was characterized at pH 7, 37 °C, and 3T. A series of B_1 values from 0.6 μT to 3.0 μT were tested, and corresponding Z-spectra and CEST contrasts are shown in Figure 2a and b. Two unique CEST contrasts were observed at 4.2 ppm and −3.4 ppm, which was generated by the amide protons of iopamidol as shown in Figure 1c and the phospholipid bilayer of liposomes as shown in our previous study, respectively.[51] Interestingly, we did not observe the other amide proton of iopamidol in Iop-lipobeads at pH > 7 at 3T. This could be attributed to the different water accessibility and exchange environment in microbeads. Moreover, we acquired the CEST at 3T; the spectral resolution might not be high enough to resolve the peak reliably at 5.6 ppm. Thus, we used CEST contrast at 4.2 ppm for pHe measurement. At 4.2 ppm, CEST contrast increased with the B_1 first and reached an optimal value of 11.5 ± 0.6% at B_1 = 1.6 μT (Figure 2c). The highest CEST contrast at 4.2 ppm was measured at 1.6 μT and 2.0 μT. At B_1 = 1.6 μT, CEST contrast at −3.4 ppm showed a relatively high signal of 2.2 ± 0.2% and drastically decreased to −0.6 ± 0.4% when the B_1 further increased to 3.0 μT. Thus, an optimal B_1 of 1.6 μT was used for phantom study. We then studied the retention of iopamidol in liposomal microbeads. Stable CEST contrast at 4.2 ppm was detected in Iop-lipobeads for 20 days with daily replacement of saline at 37 °C, as shown in Figure 2d. This showed a substantial retention of iopamidol when compared to other CT CAs in liposomes (~75% release in 24 h[59]) or in alginate hydrogel (>90% release within 100 min[60]). This suggested great potential of our Iop-lipobeads for longitudinal monitoring in vivo.

pH Dependency of Iop-Lipobeads in Vitro. We then examined the pH dependency at a range of 6.0 to 8.0 and the pH sensitivity of CEST contrast at 4.2 ppm of Iop-lipobeads in cell culture mediums, which mimicked the pH changes in the extracellular environment. At 4.2 ppm, an increase in pH from 6.0 to 7.0 resulted in an increase in CEST contrast (Figure 3). The CEST contrast at 4.2 ppm acquired at B_1 = 1.6 μT was 10.7% at a pH of 7.0. CEST contrast increases in percentage in Iop-lipobeads at 6.5−7.0 pH was 13.4%, which was attributed to an increase in the exchange rate at pH 7.0 from that at pH 6.5[61] because amide protons of iopamidol were a base-catalyzed exchange.[20,62] The sensitivity of CEST at 4.2 ppm of Iop-lipobeads was relatively lower compared with the iopamidol solution,[28] which could be attributed to the lesser water accessibility of iopamidol in Iop-lipobeads.[44] Interestingly, the nuclear Overhauser enhancement (NOE) was not sensitive to the pH change (Figure 3c), which could be a reliable readout to indicate the concentration of liposomes. CEST contrast at 4.2 ppm is not monotonic with pH (Figure 3c), which could limit the pH measurement in normal tissue.

The pH of a set of culture media, i.e., hypoxic medium, normoxic medium, and fresh medium, was measured with both CEST contrast at 4.2 ppm and a pH meter (Figure S3). CEST contrast of the HM was about 7.8% lower than that of the normoxic/fresh medium, which was due to the decreased exchange rate in lower pH environment in hypoxic medium.[61] The measured pH was 6.8 for hypoxic medium, 7.1 for nomoxic medium, and 7.2 for fresh medium, respectively. Thus, this indicated that the Iop-lipobeads were sensitive to detecting a change of 0.3 in pH, which resembles acidosis in a tumor microenvironment.

CEST MRI of Iop-Lipobeads in Mice. We further optimized the B_1 for CEST imaging of Iop-lipobeads in vivo. This is because the exchange environment might vary in vivo due to the presence of other molecules. Figure 4 showed CEST contrast at 4.2 ppm after subcutaneous injection into mice without tumor. CEST increased from 4.6 ± 0.1% to 6.9 ± 0.5% with B_1 power increased from 0.6 μT to 1.6 μT, then decreased to 6.2 ± 0.5% at 2.0 μT, which was slightly different from that in

https://doi.org/10.1021/acsami.2c10493
ACS Appl. Mater. Interfaces 2022, 14, 54401−54410

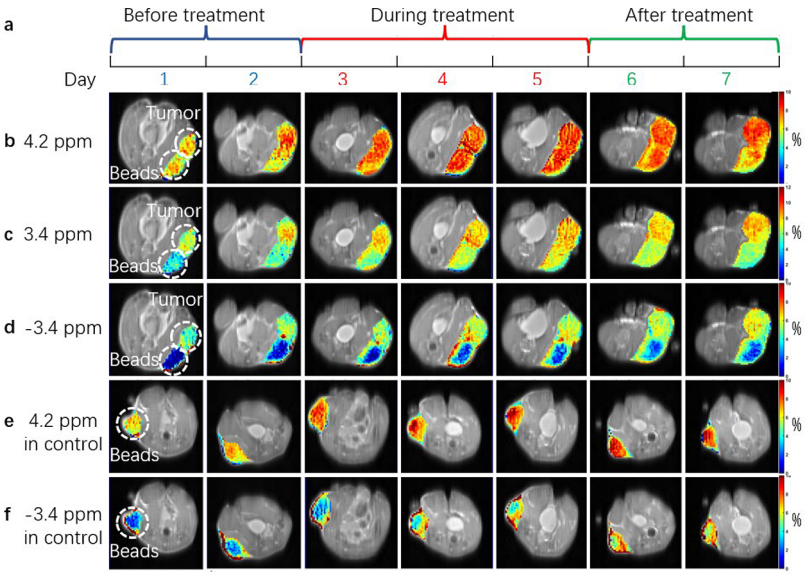

Figure 5. CEST maps in mice with or without tumors before treatment, during treatment, and after sodium bicarbonate treatment. (a) Plan for treatment. CEST maps at (b) 4.2 ppm, (c) 3.4 ppm, and (d) −3.4 ppm in a representative mouse with tumor at B_1 = 1.6 μT. CEST maps at (e) 4.2 ppm and (f) −3.4 ppm in a representative mouse without tumors.

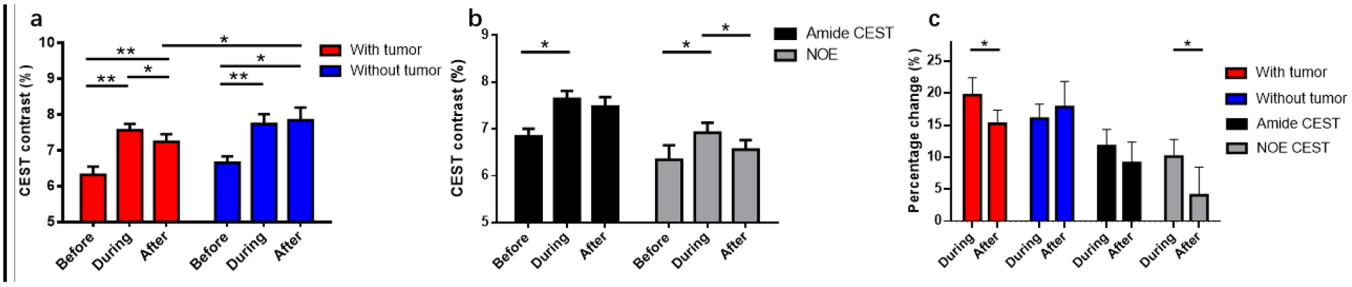

Figure 6. CEST contrast change in Iop-lipobeads and tumors in mice before, during, and after sodium bicarbonate treatment. (a) CEST contrast at 4.2 ppm in Iop-lipobeads in mice with tumors (n = 5) and without tumors (n = 4). (b) Amide CEST and NOE contrast in tumors. (c) Relative changes of CEST contrast in Iop-lipobeads in mice with and without tumors and endogenous CEST contrast, i.e., ATP and NOE, which clearly indicated a better pH sensitivity in Iop-lipobeads. The error bars represent standard errors.

vitro due to the additional magnetization transfer contribution in vivo. Moreover, the injection of Iop-lipobeads could induce inflammation in mice without tumors, which was supported by the NOE increase at the microbead periphery (Figure 5f) and the histology results (Figure 7c). NOE is sensitive to lipids/proteins, especially lipid-rich structures, e.g., the cell membrane and myelin.[25] Inflammation typically results in acidosis, thus reducing the pH of normal tissue to less than 7.0.[63,64] The B_1 power of 1.6 μT was applied for following in vivo experiments.

CEST contrasts of Iop-lipobeads in mice before, during, and after bicarbonate treatment were investigated (Figure 5). We observed an increase in CEST contrast at 4.2 ppm in the Iop-lipobead regions upon bicarbonate treatment, followed by a decrease after treatment. In mice with tumors, the CEST at 4.2 ppm of Iop-lipobeads increased from 6.3 ± 0.5% before treatment to 7.5 ± 0.4% and 7.3 ± 0.5% during and after treatment, respectively (Figures 5b and 6a). These represented a percentage increase of 19.7 ± 6.1% and 15.2 ± 4.8% during and after treatment, respectively (Figure 6c), which resembles the percentage increase (~20%) at 4.2 ppm at 3T[28] induced by a pH increment of 0.3, i.e., the reported pHe increment from previous studies with a similar treatment regime.[1,18,53] In mice without tumors, the CEST at 4.2 ppm of Iop-lipobeads increased from 6.7 ± 0.4% before treatment to 7.7 ± 0.6% and 7.9 ± 0.7% during and after treatment, respectively (Figures 5e and 6a), corresponding to an increased percentage of 16.1 ± 4.5% and 17.8 ± 8.0%, respectively (Figure 6c). We observed a substantial change of CEST contrast at −3.4 ppm of Iop-lipobeads neither in tumor bearing mice (Figure 5d) nor in mice without tumors (Figure 5f), which could support a minimal release of liposomes.

As shown in Figure 6a, the CEST contrast at 4.2 ppm of Iop-lipobeads demonstrated a significant increase during treatment in mice both without and with tumors (P < 0.01).[63,64] There was a significant decrease in CEST contrast after treatment (P < 0.05) in the tumor bearing mice (Figure 6a). The CEST contrast at 4.2 ppm after treatment in both mice with and without tumors remained high after treatment. This could be related to the poor drainage or the lesser acidosis in the tumor microenvironment after treatment and the potential release of iopamidol. Moreover, the foreign body responses could worsen the drainage in the tumor region. Thus, when comparing the percentage change of CEST contrast at 4.2 ppm, a continuous increase was observed in mice without tumors (Figure 6c), for which the percentage increase was significantly lower in mice with tumors. The estimated in vivo pH changes based on the ratiometric method can be found in Figures S4 and S5. The estimated pH in mice with tumors increased during treatment and slightly decreased after treatment, while the pH in mice

https://doi.org/10.1021/acsami.2c10493
ACS Appl. Mater. Interfaces 2022, 14, 54401−54410

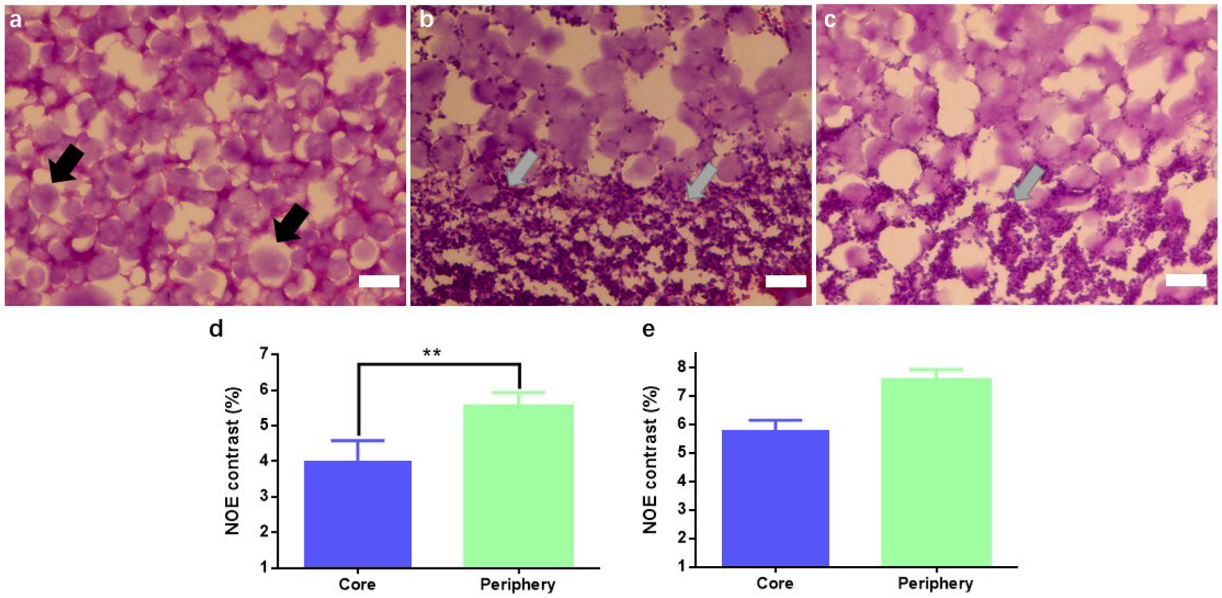

Figure 7. Hematoxylin and eosin (H&E) staining of subcutaneous Iop-lipobeads 7 days after injection. (a) The center of the Iop-lipobead region and (b) the periphery of the Iop-lipobead region in mice with tumors. (c) The periphery of the Iop-lipobeads region in mice without tumors. Scale bar: 50 μm. Comparison of NOE contrast in the Iop-lipobead regions (core vs periphery) of (d) mice with tumors and (e) mice without tumors. Black arrows and gray arrows indicated the Iop-lipobeads and cells, respectively. The error bars represent standard errors.

without tumors increased during and after treatment. This was consistent with CEST changes at 4.2 ppm in Iop-lipobeads. This also indicates the sensitivity of Iop-lipobeads in sensing pH changes in the tumor microenvironment.

Endogenous CEST contrast at 3.4 ppm (amide) and −3.4 ppm (NOE) of tumors could indicate pH changes.[22,26,65] Amide CEST in tumors was 6.9 ± 0.4%, 7.7 ± 0.4%, and 7.5 ± 0.5% and NOE in tumors was 6.3 ± 0.7%, 6.9 ± 0.5%, and 6.5 ± 0.5% before, during, and after treatment, respectively (Figure 6b). There were percentage increases of 11.7 ± 5.8% and 9.1 ± 7.3% for amide CEST and 9.6 ± 6.0% and 4.1 ± 9.8% for NOE during and after treatment, respectively (Figure 6c).[66] The increase during treatment and decrease after treatment in amide CEST was consistent with reported findings that amide CEST was increased with pH.[22] Notably, percentage changes of CEST at 4.2 ppm in Iop-lipobeads were higher than that of amide CEST in tumors during and after treatment (Figure 6c), which strongly supported the sensitivity and specificity of the Iop-lipobeads in detecting pHe changes during tumor treatment.

Histology Study. We performed H&E staining to study the changes at tissue level related to the injection of Iop-lipobeads. We observed the Iop-lipobeads with sizes comparable to in vitro (Figure 7a) and a relatively higher number of cells at the periphery of the Iop-lipobead region in mice both with (Figure 7b) and without tumors (Figure 7c). The NOE contrast of the periphery of the Iop-lipobead region was 5.6%, and it is significantly higher ($P < 0.01$) than that of the core of the Iop-lipobead region (i.e., 4.0%; Figure 7d). With reference to a previous study,[45] fewer immune responses related to the foreign body responses were observed in Iop-lipobeads, with less of a layer of cells around the Iop-lipobead region (Figure 7). This could be due to the much smaller alginate microbeads being used in this study (35.6 μm) when compared with 300−400 μm in the previous study.[45] Although this immune response is inevitably observed with alginate hydrogel injection,[43,45] we could control the size and dispersity to minimize the response.

CONCLUSION

In this study, we demonstrated the feasibility of monitoring pHe change during tumor bicarbonate treatment with pH sensitive Iop-lipobeads. The customized microfluidic device enables the generation of Iop-lipobeads at a range of 35.6−54.5 μm. The microbeads of 35.6 μm showed stable CEST contrast at 4.2 ppm of 10.6% for 20 days and changed by 13.4% at 6.5−7.0 pH in vitro. This pH sensitivity enables the identification of a hypoxic medium and normoxic medium. In tumor mice, CEST at 4.2 ppm in Iop-lopobeads increased by 19.7% during the 3 days of treatment, while it decreased by 15.2% after treatment. The endogenous amide CEST could indicate the pH changes in tumors, thus reflecting the tumor responses. Interestingly, amide CEST only changed by 11.7% and 9.1% during and after treatment, respectively. The CEST change percentage in Iop-lipobeads was higher than the endogenous CEST change percentage in tumors. This indicated that Iop-lipobeads are sensitive to pH changes in tumor microenvironment (pHe), which could independently reveal the treatment effect on pHe. Moroever, the endogenous CEST contrast could serve as additional contrast to assess the responses of tumors toward the treatment. These results demonstrated that the Iop-lipobead could provide an independent assessment of the pH changes for a noninvasive and longitudinal monitoring of the treatment effects, especially using multiple CEST contrast.

ASSOCIATED CONTENT

Supporting Information

The Supporting Information is available free of charge at https://pubs.acs.org/doi/10.1021/acsami.2c10493.

Bright field images for Iop-lipobeads prepared by microfluidics at different flow rates (Figure S1); Z-spectra and CEST contrast for iopamidol liposome at varied B_1 power and B_1 power dependency of NOE in liposomes in vitro at neutral pH (Figure S2); CEST properties of Iop-lipobeads in different media (Figure S3); fitted pH

https://doi.org/10.1021/acsami.2c10493
ACS Appl. Mater. Interfaces 2022, 14, 54401−54410

calibration curve using a ratiometric approach and CEST signal at 4.2 ppm (Figure S4); estimated pH of Iop-lipobeads in mice with and without tumors using a ratiometric approach (Figure S5) (PDF)

AUTHOR INFORMATION

Corresponding Author

Kannie W. Y. Chan − *Department of Biomedical Engineering, City University of Hong Kong, Hong Kong, China; City University of Hong Kong Shenzhen Research Institute, Shenzhen, China; Russell H. Morgan Department of Radiology and Radiological Science, The Johns Hopkins University School of Medicine, Baltimore, Maryland 21205, United States; Tung Biomedical Sciences Centre, City University of Hong Kong, Hong Kong, China; Hong Kong Centre for Cerebro-Cardiovascular Health Engineering, Hong Kong, China;* orcid.org/0000-0002-7315-1550; Email: KannieW.Y.C@cityu.edu.hk

Authors

Peng Xiao − *Department of Biomedical Engineering, City University of Hong Kong, Hong Kong, China*

Jianpan Huang − *Department of Biomedical Engineering, City University of Hong Kong, Hong Kong, China*

Xiongqi Han − *Department of Biomedical Engineering, City University of Hong Kong, Hong Kong, China;* orcid.org/0000-0003-3557-0268

Jacinth W. S. Cheu − *Department of Pathology, Li Ka Shing Faculty of Medicine, The University of Hong Kong, Hong Kong, China*

Yang Liu − *Department of Biomedical Engineering, City University of Hong Kong, Hong Kong, China*

Lok Hin Law − *Department of Biomedical Engineering, City University of Hong Kong, Hong Kong, China*

Joseph H. C. Lai − *Department of Biomedical Engineering, City University of Hong Kong, Hong Kong, China*

Jiyu Li − *Department of Biomedical Engineering, City University of Hong Kong, Hong Kong, China*

Se Weon Park − *Department of Biomedical Engineering, City University of Hong Kong, Hong Kong, China*

Carmen C. L. Wong − *Department of Pathology, Li Ka Shing Faculty of Medicine, The University of Hong Kong, Hong Kong, China; State Key Laboratory of Liver Research, The University of Hong Kong, Hong Kong, China*

Raymond H. W. Lam − *Department of Biomedical Engineering, City University of Hong Kong, Hong Kong, China;* orcid.org/0000-0002-5188-3830

Complete contact information is available at: https://pubs.acs.org/10.1021/acsami.2c10493

Funding

Research Grants Council: 11102218, PDFS2122-1S01, C1134-20G; City University of Hong Kong: 7005433, 7005626, 9667198, 9609307, and 9610560; National Natural Science Foundation of China: 81871409; Tung Foundation; Hong Kong Centre for Cerebro-Cardiovascular Health Engineering.

Notes

The authors declare no competing financial interest.

REFERENCES

(1) Estrella, V.; Chen, T.; Lloyd, M.; Wojtkowiak, J.; Cornnell, H. H.; Ibrahim-Hashim, A.; Bailey, K.; Balagurunathan, Y.; Rothberg, J. M.; Sloane, B. F.; Johnson, J.; Gatenby, R. A.; Gillies, R. J. Acidity Generated by the Tumor Microenvironment Drives Local Invasion. *Cancer Res.* **2013**, *73* (5), 1524−1535.

(2) Gillies, R. J.; Gatenby, R. A. Hypoxia and Adaptive Landscapes in the Evolution of Carcinogenesis. *Cancer Metastasis Rev.* **2007**, *26* (2), 311−317.

(3) Shi, Q.; Le, X.; Wang, B.; Abbruzzese, J. L.; Xiong, Q.; He, Y.; Xie, K. Regulation of Vascular Endothelial Growth Factor Expression by Acidosis in Human Cancer Cells. *Oncogene* **2001**, *20* (28), 3751−3756.

(4) Bix, G.; Castello, R.; Burrows, M.; Zoeller, J. J.; Weech, M.; Iozzo, R. A.; Cardi, C.; Thakur, M. L.; Barker, C. A.; Camphausen, K.; Iozzo, R. V. Endorepellin in Vivo: Targeting the Tumor Vasculature and Retarding Cancer Growth and Metabolism. *J. Natl. Cancer Inst.* **2006**, *98* (22), 1634−1646.

(5) Raghunand, N.; He, X.; van Sluis, R.; Mahoney, B.; Baggett, B.; Taylor, C.; Paine-Murrieta, G.; Roe, D.; Bhujwalla, Z.; Gillies, R. Enhancement of Chemotherapy by Manipulation of Tumour pH. *Br. J. Cancer* **1999**, *80* (7), 1005−1011.

(6) Trédan, O.; Galmarini, C. M.; Patel, K.; Tannock, I. F. Drug Resistance and the Solid Tumor Microenvironment. *J. Natl. Cancer Inst.* **2007**, *99* (19), 1441−1454.

(7) Anemone, A.; Consolino, L.; Arena, F.; Capozza, M.; Longo, D. L. Imaging Tumor Acidosis: A Survey of the Available Techniques for Mapping in Vivo Tumor pH. *Cancer Metastasis Rev.* **2019**, *38* (1−2), 25−49.

(8) Gatenby, R. A.; Gillies, R. J. Why Do Cancers Have High Aerobic Glycolysis? *Nat. Rev. Cancer* **2004**, *4* (11), 891−899.

(9) Corbet, C.; Feron, O. Tumour Acidosis: From the Passenger to the Driver's Seat. *Nat. Rev. Cancer* **2017**, *17* (10), 577−593.

(10) Muller-Lutz, A.; Khalil, N.; Schmitt, B.; Jellus, V.; Pentang, G.; Oeltzschner, G.; Antoch, G.; Lanzman, R. S.; Wittsack, H. J. Pilot study of Iopamidol-based quantitative pH imaging on a clinical 3T MR scanner. *MAGMA* **2014**, *27* (6), 477−485.

(11) Kombala, C. J.; Kotrotsou, A.; Schuler, F. W.; De La Cerda, J.; Ma, J. C.; Zhang, S.; Pagel, M. D. Development of a Nanoscale Chemical Exchange Saturation Transfer Magnetic Resonance Imaging Contrast Agent That Measures pH. *ACS Nano* **2021**, *15* (12), 20678−20688.

(12) Dong, X.; Chi, J.; Shao, C.; Lei, L.; Yang, L.; Zhao, C.; Liu, H. Multifunctional Hydrogel Microsphere with Reflection in near-Infrared Region for in Vivo pH Monitoring and Drug Release in Tumor Microenvironment. *Chemical Engineering Journal* **2021**, *421*, 127873.

(13) Jo, J.; Lee, C. H.; Kopelman, R.; Wang, X. In Vivo Quantitative Imaging of Tumor pH by Nanosonophore Assisted Multispectral Photoacoustic Imaging. *Nat. Commun.* **2017**, *8* (1), 1−10.

(14) Demoin, D. W.; Wyatt, L. C.; Edwards, K. J.; Abdel-Atti, D.; Sarparanta, M.; Pourat, J.; Longo, V. A.; Carlin, S. D.; Engelman, D. M.; Andreev, O. A.; Reshetnyak, Y. K.; Viola-Villegas, N.; Lewis, J. S. PET Imaging of Extracellular pH in Tumors with ^{64}Cu- and ^{18} F-Labeled pHLIP Peptides: A Structure−Activity Optimization Study. *Bioconjugate Chem.* **2016**, *27* (9), 2014−2023.

(15) Gillies, R.; Liu, Z.; Bhujwalla, Z. 31P-MRS Measurements of Extracellular pH of Tumors Using 3-Aminopropylphosphonate. *Am. J. Physiol. Cell Physiol.* **1994**, *267* (1), C195−C203.

(16) Smith, S.; Griffiths, R.; Martin, P.; Edwards, R. Measurement of Tumor pH with in Vivo Mr Spectroscopy. *Radiology* **1989**, *173* (2), 572−573.

(17) Gallagher, F. A.; Kettunen, M. I.; Day, S. E.; Hu, D.-E.; Ardenkjær-Larsen, J. H.; 't Zandt, R. i.; Jensen, P. R.; Karlsson, M.; Golman, K.; Lerche, M. H.; Brindle, K. M. Magnetic Resonance Imaging of pH in Vivo Using Hyperpolarized ^{13}C-Labelled Bicarbonate. *Nature* **2008**, *453* (7197), 940−943.

(18) Chen, L. Q.; Howison, C. M.; Jeffery, J. J.; Robey, I. F.; Kuo, P. H.; Pagel, M. D. Evaluations of Extracellular pH within in Vivo Tumors Using Acidocest MRI. *Magn Reson Med.* **2014**, *72* (5), 1408−1417.

(19) McVicar, N.; Li, A. X.; Goncalves, D. F.; Bellyou, M.; Meakin, S. O.; Prado, M. A.; Bartha, R. Quantitative Tissue pH Measurement During Cerebral Ischemia Using Amine and Amide Concentration-

Independent Detection (AACID) with MRI. *J. Cereb Blood Flow Metab* **2014**, *34* (4), 690−8.
(20) Moon, B. F.; Jones, K. M.; Chen, L. Q.; Liu, P.; Randtke, E. A.; Howison, C. M.; Pagel, M. D. A Comparison of Iopromide and Iopamidol, Two Acidocest Mri Contrast Media That Measure Tumor Extracellular pH. *Contrast Media Mol. Imaging* **2015**, *10* (6), 446−55.
(21) Lombardi, A. F.; Wong, J. H.; High, R.; Ma, Y.; Jerban, S.; Tang, Q.; Du, J.; Frost, P.; Pagel, M. D.; Chang, E. Y. AcidoCEST MRI Evaluates the Bone Microenvironment in Multiple Myeloma. *Mol. Imaging Biol.* **2021**, *23* (6), 865−873.
(22) Zhou, J.; Payen, J.-F.; Wilson, D. A.; Traystman, R. J.; van Zijl, P. Using the Amide Proton Signals of Intracellular Proteins and Peptides to Detect pH Effects in MRI. *Nat. Med.* **2003**, *9* (8), 1085−1090.
(23) Sagiyama, K.; Mashimo, T.; Togao, O.; Vemireddy, V.; Hatanpaa, K. J.; Maher, E. A.; Mickey, B. E.; Pan, E.; Sherry, A. D.; Bachoo, R. M.; Takahashi, M. In Vivo Chemical Exchange Saturation Transfer Imaging Allows Early Detection of a Therapeutic Response in Glioblastoma. *Proc. Natl. Acad. Sci. U. S. A.* **2014**, *111* (12), 4542−4547.
(24) Zhou, J.; Tryggestad, E.; Wen, Z.; Lal, B.; Zhou, T.; Grossman, R.; Wang, S.; Yan, K.; Fu, D.-X.; Ford, E.; Tyler, B.; Blakeley, J.; Laterra, J.; van Zijl, P. C M Differentiation between Glioma and Radiation Necrosis Using Molecular Magnetic Resonance Imaging of Endogenous Proteins and Peptides. *Nat. Med.* **2011**, *17* (1), 130−134.
(25) Huang, J.; Chen, Z.; Park, S.-W.; Lai, J. H.; Chan, K. W. Molecular Imaging of Brain Tumors and Drug Delivery Using Cest Mri: Promises and Challenges. *Pharmaceutics* **2022**, *14* (2), 451.
(26) Ray, K. J.; Simard, M. A.; Larkin, J. R.; Coates, J.; Kinchesh, P.; Smart, S. C.; Higgins, G. S.; Chappell, M. A.; Sibson, N. R. Tumor pH and Protein Concentration Contribute to the Signal of Amide Proton Transfer Magnetic Resonance Imaging. *Cancer Res.* **2019**, *79* (7), 1343−1352.
(27) Jin, T.; Wang, P.; Zong, X.; Kim, S. G. MR Imaging of the Amide-Proton Transfer Effect and the pH-Insensitive Nuclear Overhauser Effect at 9.4 T. *Magn Reson Med.* **2013**, *69* (3), 760−770.
(28) Longo, D. L.; Bartoli, A.; Consolino, L.; Bardini, P.; Arena, F.; Schwaiger, M.; Aime, S. In Vivo Imaging of Tumor Metabolism and Acidosis by Combining PET and MRI-CEST pH Imaging. *Cancer Res.* **2016**, *76* (22), 6463−6470.
(29) Goldenberg, J. M.; Cardenas-Rodriguez, J.; Pagel, M. D. Preliminary Results That Assess Metformin Treatment in a Preclinical Model of Pancreatic Cancer Using Simultaneous [^{18}F]FDG PET and Acidocest Mri. *Mol. Imaging Biol.* **2018**, *20* (4), 575−583.
(30) Jones, K. M.; Randtke, E. A.; Yoshimaru, E. S.; Howison, C. M.; Chalasani, P.; Klein, R. R.; Chambers, S. K.; Kuo, P. H.; Pagel, M. D. Clinical Translation of Tumor Acidosis Measurements with Acidocest MRI. *Mol. Imaging Biol.* **2017**, *19* (4), 617−625.
(31) Aime, S.; Calabi, L.; Biondi, L.; De Miranda, M.; Ghelli, S.; Paleari, L.; Rebaudengo, C.; Terreno, E. Iopamidol: Exploring the Potential Use of a Well-Established X-Ray Contrast Agent for Mri. *Magn Reson Med.* **2005**, *53* (4), 830−4.
(32) Consolino, L.; Anemone, A.; Capozza, M.; Carella, A.; Irrera, P.; Corrado, A.; Dhakan, C.; Bracesco, M.; Longo, D. L. Non-Invasive Investigation of Tumor Metabolism and Acidosis by MRI-CEST Imaging. *Front. Oncol.* **2020**, *10*, 161.
(33) Prasad, S.; Chandra, A.; Cavo, M.; Parasido, E.; Fricke, S.; Lee, Y.; D'Amone, E.; Gigli, G.; Albanese, C.; Rodriguez, O.; Del Mercato, L. L. Optical and Magnetic Resonance Imaging Approaches for Investigating the Tumour Microenvironment: State-of-the-Art Review and Future Trends. *Nanotechnology* **2021**, *32* (6), 062001.
(34) Lindeman, L. R.; Randtke, E. A.; High, R. A.; Jones, K. M.; Howison, C. M.; Pagel, M. D. A Comparison of Exogenous and Endogenous CEST MRI Methods for Evaluating in Vivo pH. *Magn Reson Med.* **2018**, *79* (5), 2766−2772.
(35) Anemone, A.; Consolino, L.; Conti, L.; Reineri, F.; Cavallo, F.; Aime, S.; Longo, D. L. In Vivo Evaluation of Tumour Acidosis for Assessing the Early Metabolic Response and Onset of Resistance to Dichloroacetate by Using Magnetic Resonance pH Imaging. *Int. J. Oncol.* **2017**, *51* (2), 498−506.
(36) High, R. A.; Randtke, E. A.; Jones, K. M.; Lindeman, L. R.; Ma, J. C.; Zhang, S.; LeRoux, L. G.; Pagel, M. D. Extracellular Acidosis Differentiates Pancreatitis and Pancreatic Cancer in Mouse Models Using AcidoCEST MRI. *Neoplasia* **2019**, *21* (11), 1085−1090.
(37) Lindeman, L. R.; Jones, K. M.; High, R. A.; Howison, C. M.; Shubitz, L. F.; Pagel, M. D. Differentiating Lung Cancer and Infection Based on Measurements of Extracellular pH with AcidoCEST MRI. *Sci. Rep* **2019**, *9* (1), 13002.
(38) Anemone, A.; Consolino, L.; Conti, L.; Irrera, P.; Hsu, M. Y.; Villano, D.; Dastru, W.; Porporato, P. E.; Cavallo, F.; Longo, D. L. Tumour acidosis evaluated in vivo by MRI-CEST pH imaging reveals breast cancer metastatic potential. *Br. J. Cancer* **2021**, *124*, 207−216.
(39) Cheng, W.; Zhao, F.; Tang, C. Y.; Li, X. W.; Luo, M.; Duan, S. B. Comparison of Iohexol and Iodixanol Induced Nephrotoxicity, Mitochondrial Damage and Mitophagy in a New Contrast-Induced Acute Kidney Injury Rat Model. *Arch. Toxicol.* **2018**, *92* (7), 2245−2257.
(40) Dhamecha, D.; Movsas, R.; Sano, U.; Menon, J. U. Applications of Alginate Microspheres in Therapeutics Delivery and Cell Culture: Past, Present and Future. *Int. J. Pharm.* **2019**, *569*, 118627.
(41) Mazzitelli, S.; Capretto, L.; Quinci, F.; Piva, R.; Nastruzzi, C. Preparation of Cell-Encapsulation Devices in Confined Microenvironment. *Adv. Drug Deliv Rev.* **2013**, *65* (11−12), 1533−55.
(42) Yu, L.; Sun, Q.; Hui, Y.; Seth, A.; Petrovsky, N.; Zhao, C. X. Microfluidic Formation of Core-Shell Alginate Microparticles for Protein Encapsulation and Controlled Release. *J. Colloid Interface Sci.* **2019**, *539*, 497−503.
(43) Chan, K. W.; Liu, G.; Song, X.; Kim, H.; Yu, T.; Arifin, D. R.; Gilad, A. A.; Hanes, J.; Walczak, P.; van Zijl, P. C.; Bulte, J. W.; McMahon, M. T. MRI-Detectable pH Nanosensors Incorporated into Hydrogels for in Vivo Sensing of Transplanted-Cell Viability. *Nat. Mater.* **2013**, *12* (3), 268−75.
(44) Zhao, J. M.; Har-el, Y.-e.; McMahon, M. T.; Zhou, J.; Sherry, A. D.; Sgouros, G.; Bulte, J. W.; Van Zijl, P. C. Size-Induced Enhancement of Chemical Exchange Saturation Transfer (CEST) Contrast in Liposomes. *J. Am. Chem. Soc.* **2008**, *130* (15), 5178−5184.
(45) Chan, K. W.; Liu, G.; van Zijl, P. C.; Bulte, J. W.; McMahon, M. T. Magnetization Transfer Contrast MRI for Non-Invasive Assessment of Innate and Adaptive Immune Responses against Alginate-Encapsulated Cells. *Biomaterials* **2014**, *35* (27), 7811−8.
(46) Lopez-Mendez, T. B.; Santos-Vizcaino, E.; Pedraz, J. L.; Orive, G.; Hernandez, R. M. Cell Microencapsulation Technologies for Sustained Drug Delivery: Latest Advances in Efficacy and Biosafety. *J. Control. Release* **2021**, *335*, 619−636.
(47) Utech, S.; Prodanovic, R.; Mao, A. S.; Ostafe, R.; Mooney, D. J.; Weitz, D. A. Microfluidic Generation of Monodisperse, Structurally Homogeneous Alginate Microgels for Cell Encapsulation and 3d Cell Culture. *Adv. Healthc Mater.* **2015**, *4* (11), 1628−33.
(48) Xia, Y.; Whitesides, G. M. Soft Lithography. *Angew. Chem., Int. Ed.* **1998**, *37* (5), 550−575.
(49) Ren, J.; Li, J.; Li, Y.; Xiao, P.; Liu, Y.; Tsang, C. M.; Tsao, S.-W.; Lau, D.; Chan, K. W.; Lam, R. H. Elasticity-Modulated Microbeads for Classification of Floating Normal and Cancer Cells Using Confining Microchannels. *ACS Biomater. Sci. Eng.* **2019**, *5*, 3889.
(50) Chan, K. W.; Yu, T.; Qiao, Y.; Liu, Q.; Yang, M.; Patel, H.; Liu, G.; Kinzler, K. W.; Vogelstein, B.; Bulte, J. W.; van Zijl, P. C.; Hanes, J.; Zhou, S.; McMahon, M. T. A Diacest Mri Approach for Monitoring Liposomal Accumulation in Tumors. *J. Control. Release* **2014**, *180*, 51−9.
(51) Han, X.; Huang, J.; To, A. K.; Lai, J. H.; Xiao, P.; Wu, X.; Xu, J.; Chan, K. W. Cest Mri Detectable Liposomal Hydrogels for Multiparametric Monitoring in the Brain at 3t. *Theranostics* **2020**, *10* (5), 2215.
(52) Jones, C. K.; Polders, D.; Hua, J.; Zhu, H.; Hoogduin, H. J.; Zhou, J.; Luijten, P.; Van Zijl, P. C. In Vivo Three-Dimensional Whole-Brain Pulsed Steady-State Chemical Exchange Saturation Transfer at 7 T. *Magn Reson Med.* **2012**, *67* (6), 1579−1589.
(53) Robey, I. F.; Baggett, B. K.; Kirkpatrick, N. D.; Roe, D. J.; Dosescu, J.; Sloane, B. F.; Hashim, A. I.; Morse, D. L.; Raghunand, N.;

Gatenby, R. A.; Gillies, R. J. Bicarbonate Increases Tumor pH and Inhibits Spontaneous Metastases. *Cancer Res.* **2009**, *69* (6), 2260−2268.
(54) Fischer, A. H.; Jacobson, K. A.; Rose, J.; Zeller, R. Hematoxylin and Eosin Staining of Tissue and Cell Sections. *Cold Spring Harb. Protoc.* **2008**, *2008* (5), pdb.prot4986.
(55) Rezakhani, L.; Alizadeh, M.; Alizadeh, A. A Three Dimensional in Vivo Model of Breast Cancer Using a Thermosensitive Chitosan-Based Hydrogel and 4 T1 Cell Line in Balb/C. *J. Biomed Mater. Res. A* **2021**, *109* (7), 1275−1285.
(56) Takagi, I.; Shimizu, H.; Yotsuyanagi, T. Application of Alginate Gel as a Vehicle for Liposomes. I. Factors Affecting the Loading of Drug-Containing Liposomes and Drug Release. *Chem. Pharm. Bull.* **1996**, *44* (10), 1941−1947.
(57) Chan, K. W.; Bulte, J. W.; McMahon, M. T. Diamagnetic Chemical Exchange Saturation Transfer (Diacest) Liposomes: Physicochemical Properties and Imaging Applications. *Wiley Interdiscip Rev. Nanomed Nanobiotechnol* **2014**, *6* (1), 111−24.
(58) Sun, R.; Xia, Q. Release Mechanism of Lipid Nanoparticles Immobilized within Alginate Beads Influenced by Nanoparticle Size and Alginate Concentration. *Colloid Polym. Sci.* **2019**, *297* (9), 1183−1198.
(59) Chen, Z.; Li, Y.; Airan, R.; Han, Z.; Xu, J.; Chan, K. W. Y.; Xu, Y.; Bulte, J. W. M.; van Zijl, P. C. M.; McMahon, M. T.; Zhou, S.; Liu, G. CT and CEST MRI Bimodal Imaging of the Intratumoral Distribution of Iodinated Liposomes. *Quant. Imaging Med. Surg* **2019**, *9* (9), 1579.
(60) Hu, Y.; Wang, Q.; Wang, J.; Zhu, J.; Wang, H.; Yang, Y. Shape Controllable Microgel Particles Prepared by Microfluidic Combining External Ionic Crosslinking. *Biomicrofluidics* **2012**, *6* (2), 026502.
(61) Sun, P. Z.; Longo, D. L.; Hu, W.; Xiao, G.; Wu, R. Quantification of Iopamidol Multi-Site Chemical Exchange Properties for Ratiometric Chemical Exchange Saturation Transfer (CEST) Imaging of pH. *Phys. Med. Biol.* **2014**, *59* (16), 4493−504.
(62) Ward, K.; Balaban, R. Determination of pH Using Water Protons and Chemical Exchange Dependent Saturation Transfer (Cest). *J. Magn. Reson. Imaging* **2000**, *44* (5), 799−802.
(63) Krawczyk, C. M.; Holowka, T.; Sun, J.; Blagih, J.; Amiel, E.; DeBerardinis, R. J.; Cross, J. R.; Jung, E.; Thompson, C. B.; Jones, R. G.; Pearce, E. J. Toll-Like Receptor-Induced Changes in Glycolytic Metabolism Regulate Dendritic Cell Activation. *Blood* **2010**, *115* (23), 4742−4749.
(64) Rajamäki, K.; Nordström, T.; Nurmi, K.; Åkerman, K. E.; Kovanen, P. T.; Öörni, K.; Eklund, K. K. Extracellular Acidosis Is a Novel Danger Signal Alerting Innate Immunity Via the NIRP3 Inflammasome. *J. Biol. Chem.* **2013**, *288* (19), 13410−13419.
(65) Jones, C. K.; Huang, A.; Xu, J.; Edden, R. A.; Schar, M.; Hua, J.; Oskolkov, N.; Zaca, D.; Zhou, J.; McMahon, M. T.; Pillai, J. J.; van Zijl, P. C. Nuclear Overhauser Enhancement (NOE) Imaging in the Human Brain at 7t. *Neuroimage* **2013**, *77*, 114−24.
(66) Pilon-Thomas, S.; Kodumudi, K. N.; El-Kenawi, A. E.; Russell, S.; Weber, A. M.; Luddy, K.; Damaghi, M.; Wojtkowiak, J. W.; Mule, J. J.; Ibrahim-Hashim, A.; Gillies, R. J. Neutralization of Tumor Acidity Improves Antitumor Responses to Immunotherapy. *Cancer Res.* **2016**, *76* (6), 1381−1390.

https://doi.org/10.1021/acsami.2c10493
ACS Appl. Mater. Interfaces 2022, 14, 54401−54410